Composite Structures 187 (2018) 137–143

Contents lists available at ScienceDirect

Composite Structures

journal homepage: www.elsevier.com/locate/compstruct

Nonlinear elastodynamics of piezoelectric macro-fiber composites with interdigitated electrodes for resonant actuation

D. Tan, P. Yavarow, A. Erturk*

G.W. Woodruff School of Mechanical Engineering, Georgia Institute of Technology, Atlanta, GA, USA

ARTICLE INFO

Keywords:
Piezoelectricity
Actuation
Nonlinear
Macro-fiber composites

ABSTRACT

Macro-fiber composite (MFC) piezoelectric materials are used in a variety of applications employing the converse piezoelectric effect, ranging from morphing and bioinspired actuation to vibration control in flexible structures. Most of the existing literature to date considered linear material behavior for geometrically linear oscillations. However, in many applications, such as bioinspired locomotion using MFCs, material and geometric nonlinearities are pronounced and linear models fail to represent and predict the governing dynamics. The predominant types of nonlinearities manifested in resonant actuation of MFC cantilevers are piezoelectric softening, geometric hardening, and inertial softening. In the present work, we explore nonlinear actuation of MFC cantilevers and develop an experimentally validated mathematical framework for modeling and analysis. In the experimental setting, an in vacuo actuation scenario is considered for a broad range of voltage levels (from low to moderate values) while eliminating nonlinear fluid damping. Experiments are conducted for an MFC bimorph cantilever, and model simulations based on the method of harmonic balance are compared with experimental frequency response curves under resonant actuation. The resulting experimentally validated framework can be used for simulating the dynamics of MFCs under resonant actuation, as well as parameter identification and structural optimization for linear to moderately nonlinear regime.

1. Introduction

Utilizing the piezoelectric effect for applications in bending is typically considered via the 31-mode with uniform electrodes, as is seen in applications for energy harvesting, sensing, and actuation for the past three decades [1–8]. Although the piezoelectric constant associated with the 33-mode is 50–100% larger than the piezoelectric constant associated with the 31-mode, the 33-mode has conventionally been studied for axial deformations through piezoelectric stacks for high force and low displacement applications [9–12].

Interdigitated electrodes (IDEs) with piezoelectric fibers was first explored by Bent and Hagood [13–15] for use in active-fiber composite (AFC) structures, and further studied numerically and experimentally by others [16–18]. The AFCs utilized piezoelectric fibers with circular cross sections, which limited the contact between the electrode and the piezoelectric fibers, resulting in lower electromechanical coupling and higher dielectric losses. The Macro-Fiber Composite (MFC) technology was introduced by researchers at the NASA Langley Research Center [19,20] and utilized fibers with rectangular cross sectional area for improved electromechanical coupling. Additionally, the MFC technology offers a significant increase in flexibility as compared to monolithic piezoelectric materials, which enables its use in bending applications, as well as improved actuation authority. This led to applications in bio-inspired locomotion [4,21], morphing and flapping wing designs [22–25], vibration control [26], and energy harvesting [27–31].

In terms of modeling efforts applied to MFCs, Williams et al. [32–34] performed experiments to determine the mechanical properties of MFCs using modified mixing rules (i.e. rule of mixtures). Deraemaeker et al. [35] demonstrated mixing rule calculations and compared results to both experiments and manufacturer data. Shahab and Erturk [36] combined the linearized mixing rules formulation with the dynamics established in Euler–Bernoulli beam theory to develop linear electroelastodynamic equations for MFC bimorphs for energy harvesting and actuation. Nonlinear modeling of piezoelectric materials have focused on monolithic and brittle piezoelectric materials, such as seen in the recent paper by Leadenham and Erturk [37] and the works referenced there.

In the present work, a nonlinear electroelastic model is developed for an MFC bimorph under dynamic actuation by combining piezoelectric constitutive equations with nonlinear softening due to ferroelastic hysteresis [37,38], the electroelastic and dielectric properties of

* Corresponding author.
E-mail address: alper.erturk@me.gatech.edu (A. Erturk).

https://doi.org/10.1016/j.compstruct.2017.12.056
Received 14 August 2017; Received in revised form 17 December 2017; Accepted 21 December 2017
Available online 23 December 2017

the representative volume elements (RVEs) within an MFC [35,36], and the inextensibility condition for a cantilever under nonlinear strain [39]. A single mode assumption is then applied assuming resonant actuation, yielding a nonlinear lumped parameter model for the MFC bimorph. This model is then solved using the harmonic balance method [40] and validated with in vacuo dynamic actuation experiments.

2. Nonlinear electroelastic equations for an MFC bimorph cantilever under dynamic actuation

For a piezoelectric material actuated in the 33-mode (via interdigitated electrodes), the electric enthalpy density, H, can be expressed as

$$H = \frac{1}{2}c_{33}^{E}S_3^2 - \frac{1}{3}\gamma\,|S_3|\,S_3^2 - e_{33}S_3E_3 - \frac{1}{2}\varepsilon_{33}^{S}E_3^2 \tag{1}$$

where c_{33}^{E} is the elastic modulus at constant electric field, S_3 is the strain, γ is a nonlinear strain coefficient due to ferroelastic softening, e_{33} is the piezoelectric stress constant, E_3 is the electric field, and ε_{33}^{S} is the permittivity at constant strain (these material properties are defined for the thin structure and therefore reduced from the 3D constitutive equations). The strain due to bending at any point in a cantilever can be expressed as $S_3 = -z\theta_{,s}$, where θ is the angular displacement, z is the distance from the neutral axis, and the subscript $_{,s}$ refers to a spatial derivative with respect to the arclength of the beam. Although the electric field is non-uniform within the piezoelectric material, the effective electric field can be approximated by $E_3 \approx -\frac{v}{L_e} = -\frac{\dot{\lambda}}{L_e}$, where v is the voltage across the interdigitated electrodes, L_e is the distance between the interdigitated electrodes, and $\dot{\lambda}$ is the time derivative of the flux linkage.

As described by Deraemaeker et al. [35] and Shahab and Erturk [36] and illustrated in Fig. 1, the rectangular piezoelectric fibers (colored gray in Fig. 1) within an MFC are separated by passive layers of epoxy (yellow) and then embedded within Kapton film (orange) containing interdigitated copper electrodes (brown) perpendicular to the piezoelectric fibers, creating an array of repeating representative volume elements (RVEs). Each RVE is of width b_e, length L_e, and thickness h_p (as depicted on the right side of Fig. 1), and has material properties defined by the mixing rules formulation [35,36]:

$$\begin{aligned} c_{33,e}^{E} &= \nu c_{33,p}^{E} + (1-\nu)c_{33,m}^{E} \\ d_{33,e} &= \frac{1}{c_{33,e}^{E}}\nu d_{33,p}c_{33,p}^{E} \\ \varepsilon_{33,e}^{S} &= [\nu\varepsilon_{33,p}^{T} + (1-\nu)\varepsilon_{33,m}^{T}] - d_{33,e}^{2}c_{33,e}^{E} \end{aligned} \tag{2}$$

where ν is the volume fraction of PZT within a RVE (approximately 90%), ε_{33}^{T} is the permittivity under constant stress, d_{33} is the piezoelectric charge constant, and the subscripts p, m, and e correspond to the piezoelectric fiber properties, the matrix (epoxy) properties, and the equivalent properties of the RVE, respectively.

The section of the MFC covered in piezoelectric fibers contains M number of RVEs in the width direction and N_a number of RVEs in the length direction, making the active width $b_{act} = Mb_e$ and the active length $L_{act} = N_aL_e$. Part of the MFC is clamped in a way that sections of the piezoelectric fibers remain motionless and thus are not strained, so we define the clamped active length such that $L = NL_e$, where N is the number of RVEs in the length direction that are under strain.

The MFC bimorph is constructed by bonding two MFCs back-to-back (using high shear strength epoxy) and wiring them in parallel, so the total potential energy associated with the RVEs within an MFC bimorph can be written as:

$$U_p = \int_0^L \left(\frac{1}{2}EI_p\theta_{,s}^2 - \frac{1}{3}\gamma B\,|\theta_{,s}|\,\theta_{,s}^2 - \vartheta_p\dot{\lambda}[H(s)-H(s-L)]\theta_{,s} - \frac{1}{2}\frac{C_p}{NL_e}\dot{\lambda}^2\right)ds \tag{3}$$

where the overdot refers to a time derivative, $H(s)$ is the heaviside step function, and the material properties of the piezoelectric fibers within the MFC bimorph are

$$\begin{aligned} EI_p &= 2\sum_{m=1}^{M} b_e c_{33,e}\left[\frac{(h_p+h_k)^3-(h_k)^3}{3}\right] \\ B &= \sum_{m=1}^{M} b_e\left[\frac{(h_p+h_k)^4-(h_k)^4}{2}\right] \\ \vartheta_p &= 2\sum_{m=1}^{M}\frac{b_e e_{33,e}}{L_e}\left[\frac{(h_p+h_k)^2-(h_k)^2}{2}\right] = 2\sum_{m=1}^{M} e_{33,e}\frac{b_e h_p}{L_e}\left(\frac{h_p}{2}+h_k\right) \\ &\approx 2\sum_{m=1}^{M} e_{33,e}\frac{A_e h_{pc}}{L_e} \\ C_p &= 2\sum_{m=1}^{M}\sum_{n=1}^{N_a}\varepsilon_{33,e}^{S}\frac{b_e h_p}{L_e} \approx 2\sum_{m=1}^{M}\sum_{n=1}^{N_a}\varepsilon_{33,e}^{S}\frac{A_e}{L_e} \end{aligned} \tag{4}$$

where h_p and h_k correspond to the thickness of the piezoelectric layer and the Kapton layer respectively, and the effective area A_e is introduced to account for the approximation in the electric field.

Additionally, the strain energy in the kapton-copper layers is given by:

$$\begin{aligned} U_{kc} &= \int_0^L \frac{1}{2}EI_{kc}\theta_{,s}^2 ds \\ EI_{kc} &= 2\sum_{m=1}^{M} b_e(E_c\nu_c + E_k(1-\nu_c))\left[\frac{h_k^3}{3} + \frac{(2h_k+h_p)^3-(h_k+h_p)^3}{3}\right] \end{aligned} \tag{5}$$

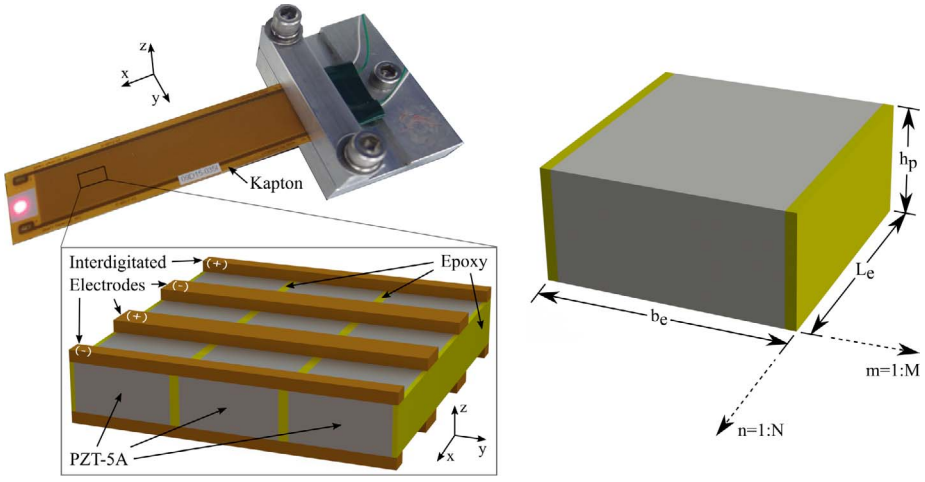

Fig. 1. MFC bimorph cantilever and a close up of one of its layers showing active piezoelectric fibers separated by epoxy and embedded in Kapton film containing interdigitated copper electrodes (left) and a representative volume element (MxN representative volume elements exist in an MFC layer) and its effective dimensions (right).

where v_c is the volume fraction of copper within the kapton-copper layer (approximately 24%), and the subscripts c, k and kc refer to the copper properties, the kapton properties, and the combined kapton-copper properties, respectively.

The total potential energy for the entire MFC bimorph can therefore be written as

$$U = \int_0^L \left(\frac{1}{2}EI_{eff}\theta_{,s}^2 - \frac{1}{3}\gamma B\,|\theta_{,s}|\,\theta_{,s}^2 - \vartheta_p\dot{\lambda}\,[H(s)-H(s-L)]\theta_{,s} - \frac{1}{2}\frac{C_p}{NL_e}\dot{\lambda}^2\right)ds \tag{6}$$

where the effective bending stiffness includes all of the RVEs and the kapton-copper layer in the MFC bimorph, $EI_{eff} = EI_p + EI_{kc}$, and the kinetic energy can be written as

$$T = \frac{1}{2}m_s\int_0^L (u_{x,t}{}^2 + u_{z,t}^2)ds \tag{7}$$

where m_s is the structural mass per length of the MFC bimorph, u_x is displacement along the length direction of the cantilever, and u_z is the transverse displacement of the cantilever.

For an inextensible cantilever, the Lagrangian needs to include a Lagrange multiplier, Λ, to account for the inextensibility condition [39,41,42]:

$$\begin{aligned}\mathscr{L} = {} & \tfrac{1}{2}m_s\int_0^L [u_{x,t}^2 + u_{z,t}^2]ds - \tfrac{1}{2}\Lambda\int_0^L [(1+u_{x,s})^2 + (u_{z,s})^2 - 1]ds + \\ & - \int_0^L \left(\tfrac{1}{2}EI_{eff}\theta_{,s}^2 - \tfrac{1}{3}\gamma B\,|\theta_{,s}|\,\theta_{,s}^2 - \vartheta_p\dot{\lambda}\,[H(s)-H(s-L)]\theta_{,s} - \tfrac{1}{2}\tfrac{C_p}{NL_e}\dot{\lambda}^2\right)ds\end{aligned} \tag{8}$$

Applying Hamilton's principle,

$$\int_{t_1}^{t_2} (\delta\mathscr{L} + \delta W_{NC})dt = 0 \tag{9}$$

where the nonconservative work on the structure includes the input electrical work necessary to actuate the MFC as well as linear structural damping,

$$\delta W_{NC} = \int_0^L (i\delta\lambda - c_z u_{z,t}\delta u_z)ds \tag{10}$$

where i is the input electrical current to the MFC bimorph, we find

$$\int_{t_1}^{t_2}\left\{\begin{array}{l}\displaystyle\int_0^L \left(\begin{array}{l} m_s u_{x,t}\delta u_{x,t} + m_s u_{z,t}\delta u_{z,t} - c_z u_{z,t}\delta u_z + \\ -\Lambda(1+u_{x,s})\delta u_{x,s} - \Lambda u_{z,s}\delta u_{z,s} + \\ +\left(\begin{array}{l}-EI_{eff}\theta_{,s} + \gamma B\theta_{,s}^2\mathrm{sgn}(\theta_{,s}) \\ +\vartheta_p\dot{\lambda}\,[H(s)-H(s-L)]\end{array}\right)\delta\theta_{,s}\end{array}\right)ds + \\ + (\int_0^L \vartheta_p\theta_{,s}\,[H(s)-H(s-L)]ds + C_p\dot{\lambda})\delta\dot{\lambda} \\ + \int_0^L i\delta\lambda ds\end{array}\right\}dt = 0 \tag{11}$$

Using integration by parts, Hamilton's principle yields 3 equations of motion with nonlinearities kept to cubic order, i.e. $O(\varepsilon^3)$:

$$\begin{aligned} m_s u_{x,tt} &= [\Lambda(1+u_{x,s}) + EI_{eff}\,(u_{z,s}u_{z,sss}) - (\vartheta_p\dot{\lambda}\,[H(s)-H(s-L)])_{,s}u_{z,s}]_{,s} \\ m_s u_{z,tt} &= \left[\begin{array}{l}\Lambda u_{z,s} - EI_{eff}\,(u_{z,sss} + u_{z,s}u_{z,ss}^2) + 2\gamma B\,|u_{z,ss}|\,u_{z,sss} + \\ +(\vartheta_p\dot{\lambda}\,[H(s)-H(s-L)])_{,s}(1+u_{x,s})\end{array}\right]_{,s} \\ & \quad - c_z u_{z,t} - \int_0^L \vartheta_p((1+u_{x,s})u_{z,ss} - u_{z,s}u_{x,ss})_{,t}ds - C_p\ddot{\lambda} + i = 0 \end{aligned} \tag{12}$$

Spatially integrating the equation for u_x and utilizing the appropriate boundary conditions, the Lagrange multiplier is obtained as:

$$\begin{aligned}\Lambda = {} & -EI_{eff}u_{z,s}u_{z,sss} - \frac{1}{2}m_s\int_L^s \left(\int_0^\delta u_{z,\xi}^2 d\xi\right)_{,tt}d\delta \\ & + (\vartheta_p\dot{\lambda}\,[H(x)-H(x-L)])_{,s}u_{z,s}\end{aligned} \tag{13}$$

which can be substituted into the equation for u_z to find

$$\begin{aligned}&\left[m_s u_{z,tt} + c_z u_{z,t} + \frac{1}{2}m_s\left[u_{z,s}\int_L^s (\int_0^\delta u_{z,\xi}^2 d\xi)_{,tt}d\delta\right]\right]_{,s} \\ &\quad + EI_{eff}\,(u_{z,sss} + u_{z,s}(u_{z,s}u_{z,ss})_{,s})_{,s} - 2\gamma B(|u_{z,ss}|\,u_{z,sss})_{,s} \\ &\quad - \vartheta_p v\left[\frac{\partial\delta(x)}{\partial s} - \frac{\partial\delta(x-L)}{\partial s}\right] - \vartheta_p v\,[\delta(x) - \delta(x-L)](u_{z,s}u_{z,ss})\Big] = 0 \\ &C_p\dot{v} - i + \int_0^L \vartheta_p\left(u_{z,ss} + \frac{1}{2}u_{z,s}^2 u_{z,ss}\right)_{,t}ds = 0\end{aligned} \tag{14}$$

If the actuation is harmonic about the first natural frequency of the structure (as a primary resonance excitation), then a single mode assumption can be made, $u_z(s,t) = \phi(s)\eta(t)$, where $\phi(s)$ is the mass normalized first bending mode shape of a cantilever,

$$\begin{aligned}&\phi(s) = A_1\left(\cos\tfrac{\lambda_1 s}{L} - \cosh\tfrac{\lambda_1 s}{L} + \sigma\left(\sin\tfrac{\lambda_1 s}{L} - \sinh\tfrac{\lambda_1 s}{L}\right)\right) \\ &\sigma = \tfrac{\sin\lambda_1 - \sinh\lambda_1}{\cos\lambda_1 + \cosh\lambda_1} \\ &\lambda_1 = 1.8751 \\ &\int_0^L m_s\phi_i(s)\phi_j(s)ds = \delta_{ij}\end{aligned} \tag{15}$$

This results in the equations of motion in modal coordinates,

$$\begin{aligned}&m^*\ddot{\eta} + c^*\dot{\eta} + k^*(1-\gamma^*\,|\eta|)\eta + \tfrac{\alpha^*}{L^2}\eta^3 + \tfrac{\beta^*}{L^2}(\eta\dot{\eta}^2 + \eta^2\ddot{\eta}) = (\theta_p + \theta_{NL}\eta^2)v \\ &i = C_p\dot{v} + \theta_p\dot{\eta} + \theta_{NL}\eta^2\dot{\eta}\end{aligned} \tag{16}$$

which can be converted back into the measurement coordinates by $w = w(L_{meas},t) = \phi(L_{meas})\eta(t)$, where L_{meas} is the distance from the base of the cantilever where the velocity is measured experimentally, yielding the final equations of motion for the MFC bimorph subject to resonant voltage excitation about the first bending mode which account for nonlinear strain, the inextensibility condition of a cantilever, and the nonlinear material softening within PZT-5A:

$$\begin{aligned}&\hat{m}\ddot{w} + \hat{c}\dot{w} + \hat{k}\,(1-\hat{\gamma}\,|w|)w + \frac{\hat{\alpha}}{L^2}w^3 + \frac{\hat{\beta}}{L^2}(w\dot{w}^2 + w^2\ddot{w}) \\ &\quad = \left(\theta_p + \frac{\theta_{NL}}{\phi^2(L_{meas})}w^2\right)v\end{aligned} \tag{17}$$

$$i = C_p\dot{v} + \frac{\theta_p}{\phi(L_{meas})}\dot{w} + \frac{\theta_{NL}}{\phi^3(L_{meas})}w^2\dot{w} \tag{18}$$

where

$$\begin{aligned}&\hat{m} = \frac{m_s\int_0^L\phi^2(s)ds}{\phi(L_{meas})\int_0^L\phi(s)ds}, && \hat{\gamma} = \frac{2\gamma B\int_0^L\phi(s)(\phi''(s)\phi'(s))'ds}{EI_{eff}\,\phi(L_{meas})\int_0^L\phi(s)\phi'''(s)ds}, \\ &\hat{c} = \frac{c_z\int_0^L\phi^2(s)ds}{\phi(L_{meas})\int_0^L\phi(s)ds}, && \hat{\alpha} = \frac{EI_{eff}L^2\int_0^L\phi(s)\{\phi'(s)(\phi'(s)\phi''(s))'\}'ds}{\phi^3(L_{meas})\int_0^L\phi(s)ds}, \\ &\hat{k} = \frac{EI_{eff}\int_0^L\phi(s)\phi'''(s)ds}{\phi(L_{meas})\int_0^L\phi(s)ds}, && \hat{\beta} = \frac{m_s L^2\int_0^L\phi(s)[\phi'(s)\int_L^s\int_0^\delta\phi'(s)^2 d\xi d\delta]'ds}{\phi^3(L_{meas})\int_0^L\phi(s)ds} \\ &\theta_p = \vartheta_p\phi'(L), && \theta_{NL} = \tfrac{1}{2}\vartheta_p(\phi'(L))^3\end{aligned} \tag{19}$$

Here, $\hat{m}$, $\hat{c}$, and $\hat{k}$ are the equivalent linear mass, damping, and stiffness terms in the lumped parameter model, $\hat{\gamma}$ is the piezoelectric softening coefficient, $\hat{\alpha}$ is the geometric hardening coefficient, $\hat{\beta}$ is the inertial softening coefficient, θ_p is the linear electromechanical coupling coefficient, and θ_{NL} is the nonlinear electromechanical coupling coefficient that is a result of nonlinear strain.

To solve Eq. (17), the method of harmonic balance [40] is used. The input electrical voltage is assumed to be harmonic of the form

$$v = V\cos(\Omega t) \tag{20}$$

where V is the voltage amplitude and Ω is the driving frequency. This results in a mechanical response solution with the same period as the electrical actuation which can be approximated by a truncated Fourier series expansion with Q harmonics,

$$w_Q = \sum_{q=1}^{Q} [a_q \cos(q\Omega t) + b_q \sin(q\Omega t)] \tag{21}$$

Substituting the approximate solution into the electromechanical equation given by Eq. (17) results in the residual function

$$R = \hat{m}\ddot{w}_Q + \hat{c}\dot{w}_Q + \hat{k}(1-\hat{\gamma}\,|w_Q|)w_Q + \frac{\hat{\alpha}}{L^2}w_Q^3 + \frac{\hat{\beta}}{L^2}(w_Q\dot{w}_Q^2 + w_Q^2\ddot{w}_Q) - \left(\theta_p + \frac{\theta_{NL}}{\phi^2(L_{meas})}w_Q^2\right)v \tag{22}$$

Then, using the Galerkin method of mean weighted residuals,

$$\begin{matrix} \int_0^{2\pi/\Omega} R\cos(q\Omega t)dt = 0 \\ \int_0^{2\pi/\Omega} R\sin(q\Omega t)dt = 0 \end{matrix} \quad q = 1,\ldots,Q \tag{23}$$

a system of $2Q$ algebraic equations for the Fourier coefficients a_q and b_q can be generated. Here we choose to include $Q = 5$ harmonics, resulting in 10 equations and 10 unknowns. These equations can be solved using a multivariate Newton–Raphson method. Because the cubic nonlinearities can result in bifurcations near resonance, the Fourier coefficients are first solved using an off-resonance driving frequency Ω, and then the driving frequency is linearly swept up and down around the resonant frequency using the previous Fourier coefficients as seed values for the Newton–Raphson method in order to capture both the high and low energy solutions of the bifurcation. Once the mechanical response of the system is known, the input actuation current is calculated using Eq. (18).

3. Experimental setup

Two MFCs, model M8507-P1 from Smart Material Corp., were vacuum bonded together without a separate substrate to form a bimorph structure, the dimensions and material properties of which are listed in Table 1. The sample was placed in an aluminum clamp and then mounted inside of a vacuum chamber at 0.01 atm as shown in Fig. 2 in order to minimize the effect of nonlinear fluid drag from the air, and the velocity of the MFC bimorph was measured near the free end of the cantilever with a Polytec OFV-505 laser Doppler vibrometer. The MFC samples in the bimorph were wired in parallel and connected to a Trek 2220 high voltage amplifier. Linear noise bursts were performed to determine the first natural frequency of the structure, which was about 40.5 Hz (in short circuit). Up and down sine sweeps were then performed between 25 and 55 Hz at 1 Hz/min for voltage amplitudes of 1 V, 5 V, and then 10 V to 100 V in 10 V intervals. The velocity response near the tip of the cantilever and the current drawn from the high voltage amplifier were recorded using an NI USB-4431 data acquisition device.

4. Results

4.1. Experimental results

Fig. 3 shows the amplitude and phase of the velocity response at the tip of the MFC bimorph to actuation near the first natural frequency as well as the required input current. Note that at a 1 V amplitude actuation level, the input electrical current was near the noise floor of the data acquisition device, so the data was plotted with dotted lines instead of a solid line for clarity. The experimental results reveal that the quadratic piezoelectric softening dominates the nonlinear behavior for all voltage levels considered. For a passive cantilevered structure excited around its first bending natural frequency, the cubic geometric hardening and inertial softening terms are expected to interact to yield a net hardening effect [43] once the mechanical response is sufficiently large, but with the introduction of the cubic electromechanical coupling term, the overall cubic nonlinearity is of a softening nature.

Table 1
Dimensions and Material Properties of the MFC Bimorph.

Property	Symbol	Value
Active length	L_{act}	85 mm
Clamped active length	L	75.5 mm
Clamped overall length	L_o	83.5 mm
Active width	b_{act}	7 mm
Total thickness	h	0.61 mm
Measured capacitance	C_p	3.40 nF
First natural frequency (SC: short circuit)	f_{SC}	40.5 Hz

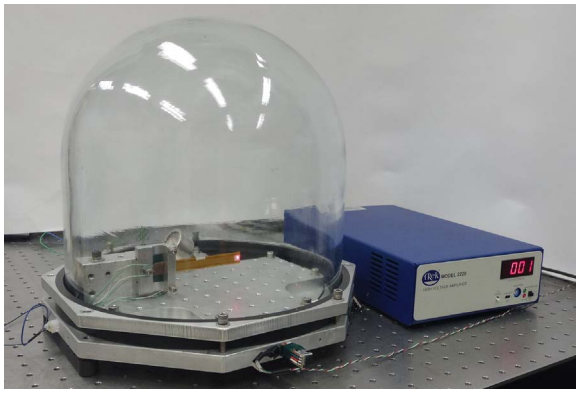

Fig. 2. Clamped MFC bimorph placed inside a vacuum chamber and connected to a high voltage amplifier for dynamic actuation.

Converting the velocity amplitude frequency response to a plot of detuning versus response amplitude in meters, a backbone curve was created by applying a polynomial fit over the points corresponding to the maximum amplitude at each actuation voltage level. This polynomial is quadratic and of the form $\sigma = C_1 a^2 + C_2 a + C_3$, where σ is the detuning and a is the response amplitude. The piezoelectric softening coefficient $\hat{\gamma}$ can be approximated by substituting a small response amplitude a_1 into the polynomial, finding the corresponding detuning σ_1, and solving

$$\hat{\gamma} = \frac{1-\left(1-\frac{\sigma_1}{\omega_n}\right)}{a_1} \tag{24}$$

which results in $\hat{\gamma} = 155.32\frac{1}{m}$. This empirical coefficient associated with ferroelastic softening was utilized in the theoretical simulations.

4.2. Theoretical results

Using the measured capacitance of the MFC bimorph (listed in Table 1), the effective area A_e was calculated to be 0.0446 mm^2. The coefficients found in Eq. (17) were then calculated using Eqs. (2), (4), and (19), as well as with the piezoelectric softening coefficient extracted from the experimental results using Eqs. (24). The nonlinear equations of motion given by Eqs. (17) were then solved using the method of harmonic balance for all voltage levels considered in the experiments. The amplitudes and phases of the velocity response and input current of the 5-term harmonic balance solution is plotted in Fig. 4.

The theoretical model shows good agreement with the trends seen in the experiments performed. All figures show that the second order piezoelectric softening due to hysteretic effects dominates the behavior through all electrical excitation levels. As the mechanical response of the MFC bimorph cantilever increases, the effective cubic hardening effect expected in a passive structure is absent due to the cubic electromechanical coupling nonlinearity and high voltage levels considered, agreeing with the observations from the experimental data.

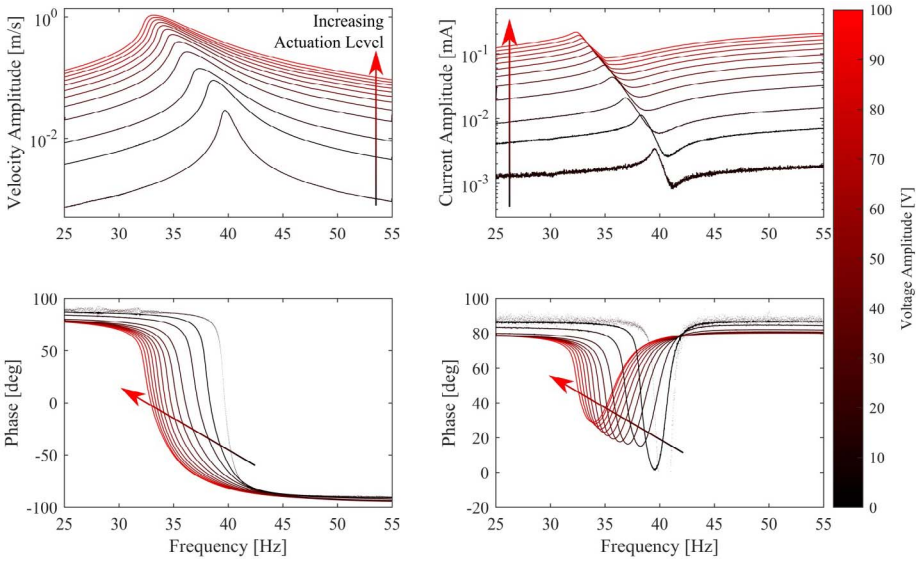

Fig. 3. Measured tip velocity and input current amplitude and phase curves of the MFC bimorph for resonant actuation with input voltage amplitudes of 1 V, 5 V, and then 10 V to 100 V in 10 V increments using a downward frequency sweep.

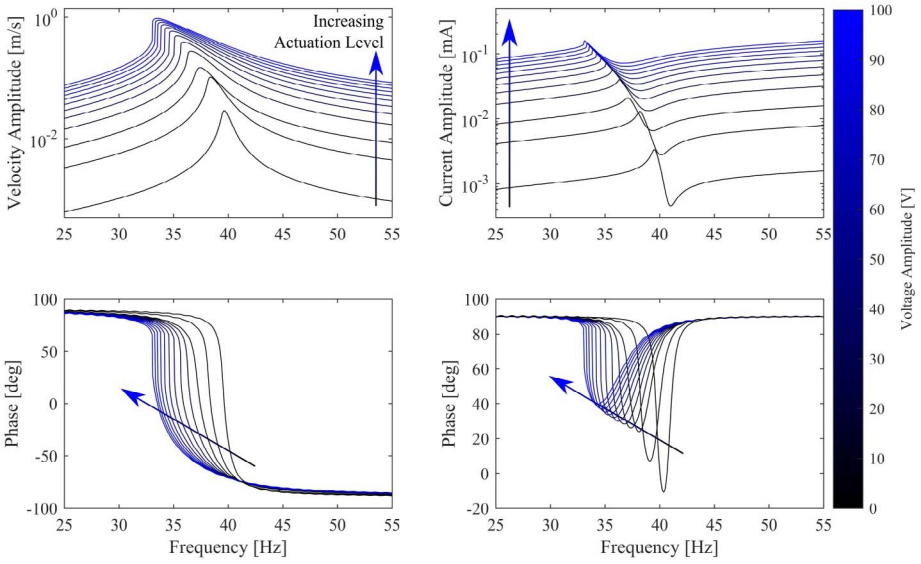

Fig. 4. Theoretical tip velocity and input current amplitude and phase curves of the MFC bimorph for resonant actuation with input voltage amplitudes of 1 V, 5 V, and then 10 V to 100 V in 10 V increments using a downward frequency sweep.

However, the theoretical results exhibit the jump phenomenon at high voltage and strain levels that are not present in the experimental results. Additional nonlinear dissipation terms need to be included in the nonlinear model in order to limit the jump phenomena at higher voltage excitation levels.

We can linearize the model by setting $\hat{\alpha}$, $\hat{\beta}$, $\hat{\gamma}$, and θ_{NL} to zero, and then compare the velocity response solutions of the linearized theoretical model to those of the nonlinear theoretical model as well as the experimental data at fixed driving frequencies for all voltage levels considered, as shown in Fig. 5. As expected, the linearized model overpredicts the mechanical response of the MFC bimorph cantilever at driving frequencies near the linear natural frequency of the structure (40.5 Hz), but underpredicts the response at frequencies below the natural frequency due to the predominant piezoelectric softening, especially at higher voltage and strain levels. Note that the significant mismatch at 33 Hz in Fig. 5 is due to the aforementioned jump behavior in the model. As the input electrical excitation level increases, the nonlinear model begins to underpredict the velocity response and the input current (see Fig. 6), indicating a need for higher order material nonlinearities which would introduce further nonlinear electromechanical coupling terms.

Due to the close spacing of the interdigitated electrodes in the MFCs ($L_e \approx 500\ \mu$m), the electric field in the piezoelectric material is approximately 200 kV/m at the highest actuation level considered in this paper. Li et al. [44] show that the piezoelectric coefficient d_{33} and the permittivity ε_{33} in soft PZT exhibit significant nonlinear behavior for electric fields greater than 25 kV/m, confirming the need for additional material nonlinearities.

5. Conclusions

In this work, a nonlinear electroelastic model was developed and experimentally validated for resonant actuation of an MFC bimorph for the first bending mode under low to moderately nonlinear actuation levels. The electroelastic properties of the MFC were calculated by combining a rule of mixtures formulation for the material properties of the representative volume element and applying Hamilton's principle

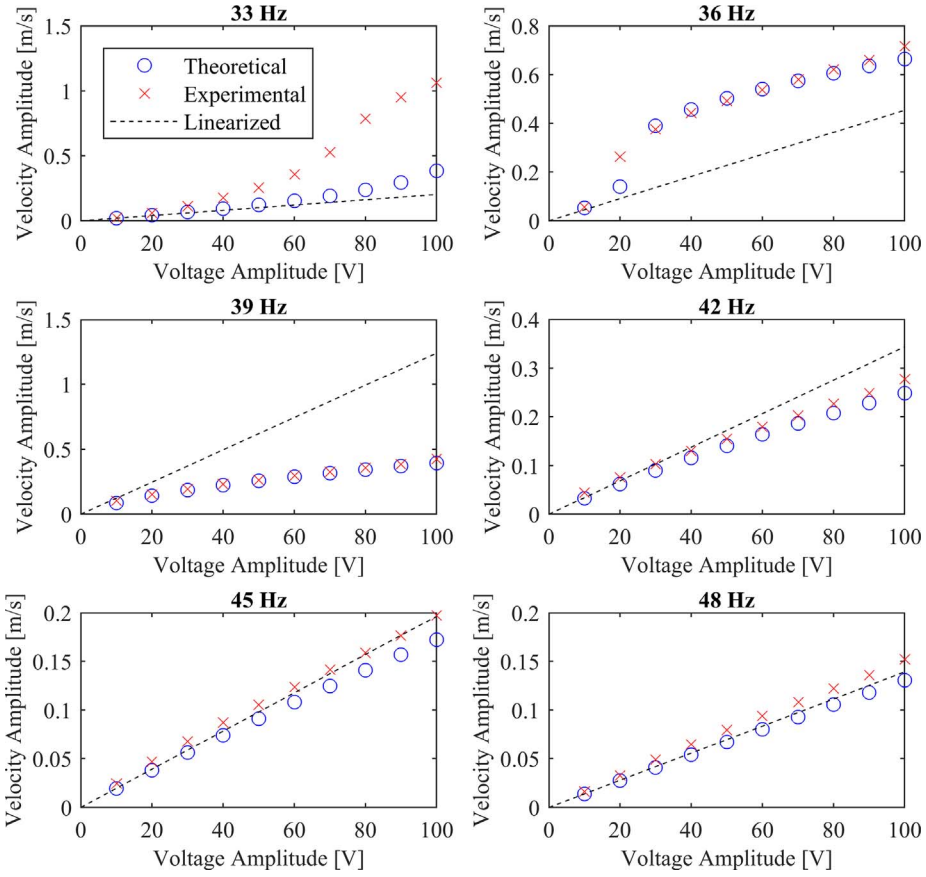

Fig. 5. Theoretical tip velocity amplitudes of the MFC bimorph as a function of input voltage amplitudes at fixed frequencies around the first natural frequency.

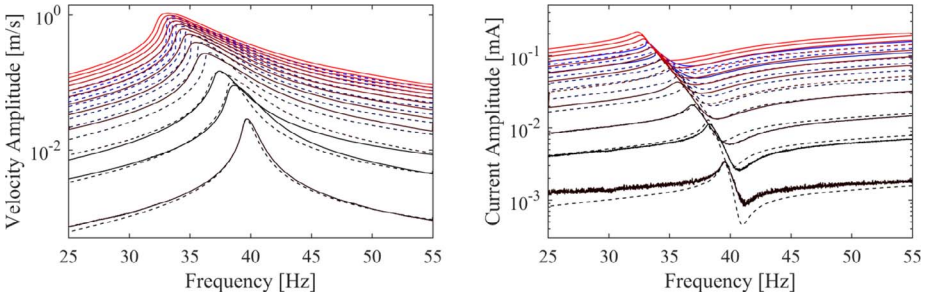

Fig. 6. A direct comparison between the theoretical (dashed lines) and experimental (solid lines) velocity and input current frequency response curves of the MFC bimorph.

on the piezoelectric constitutive equation considering nonlinear strain (with inextensibility condition) and ferroelastic softening effects. The two frequency responses of interests in resonance actuation are the vibration response and the current drawn (which can be used to quantify the actuation power consumption). The analytical model was solved using the method of harmonic balance with applied voltage amplitudes of 1–100 V and compared to experimental results. For low to moderate electrical excitation levels, the model presented accurately predicts the overall behavior of the bimorph, and it can be used for analysis and design of MFC bimorphs for applications involving resonant actuation with electric field levels similar to those considered in this work. However, as the excitation level further increases, the model gradually underpredicts the experimental results. This indicates that further work is necessary to include additional material nonlinearities for moderate to high voltage levels which introduce nonlinear dielectric and electromechanical effects. The resonant actuation experiments in this paper were conducted in a vacuum chamber, therefore linear structural damping was suffcient. Nonlinear dissipative effects (e.g. fluid drag) can easily be introduced to the model as needed.

Acknowledgments

This work was supported in part by the NSF Grant CMMI-1254262, which is gratefully acknowledged.

References

[1] Baz A, Ro J. Vibration control of plates with active constrained layer damping. Smart Mater. Struct. 1996;5(3):272.
[2] Dosch JJ, Inman DJ, Garcia E. A self-sensing piezoelectric actuator for collocated control. J Intell Mater Syst Struct 1992;3(1):166–85.
[3] Erturk A. Assumed-modes modeling of piezoelectric energy harvesters: eulerbernoulli, rayleigh, and timoshenko models with axial deformations. Comput Struct 2012;106:214–27.
[4] Erturk A, Delporte G. Underwater thrust and power generation using flexible piezoelectric composites: an experimental investigation toward self-powered swimmer-sensor platforms. Smart Mater Struct 2011;20(12):125013.
[5] Hagood NW, von Flotow A. Damping of structural vibrations with piezoelectric materials and passive electrical networks. J Sound Vib 1991;146(2):243–68.
[6] Hagood NW, Chung W, von Flotow A. Modeling of piezoelectric actuator dynamics for active structural control. J Intell Mater Syst Struct 1990;1:327–54.
[7] Leadenham S, Erturk A. Nonlinear M-shaped broadband piezoelectric energy

harvester for very low base accelerations: primary and secondary resonances. Smart Mater Struct 2015;24(5):055021.
[8] Leo DJ. Engineering analysis of smart material systems. John Wiley and Sons; 2007.
[9] Cunefare KA, Skow EA, Erturk A, Savor J, Verma N, Cacan MR. Energy harvesting from hydraulic pressure fluctuations. Smart Mater Struct 2013;22(2):025036.
[10] Feenstra J, Granstrom J, Sodano H. Energy harvesting through a backpack employing a mechanically amplified piezoelectric stack. Mech Syst Sig Process 2008;22(3):721–34.
[11] Skow EA, Cunefare KA, Erturk A. Power performance improvements for high pressure ripple energy harvesting. Smart Mater Struct 2014;23(10):104011.
[12] Zhao S, Erturk A. Deterministic and band-limited stochastic energy harvesting from uniaxial excitation of a multilayer piezoelectric stack. Sens Actuat A Phys 2014;214:58–65.
[13] Bent AA, Hagood NW. Piezoelectric fiber composites with interdigitated electrodes. J Intell Mater Syst Struct 1997;8(11):903–19.
[14] Bent AA., Active fiber composites for structural actuation, Thesis (1997).
[15] Bent AA, Hagood NW, Rodgers JP. Anisotropic actuation with piezoelectric fiber composites. J Intell Mater Syst Struct 1995;6(3):338–49.
[16] Brei D, Cannon BJ. Piezoceramic hollow fiber active composites. Compos Sci Technol 2004;64(2):245–61. http://dx.doi.org/10.1016/s0266-3538(03)00259-8.
[17] Belloli A, Niederberger D, Pietrzko S, Morari M, Ermanni P. Structural vibration control via R-L shunted active fiber composites. J Intell Mater Syst Struct 2006;18(3):275–87. http://dx.doi.org/10.1177/1045389x06066029.
[18] Lin Y, Sodano HA. Concept and model of a piezoelectric structural fiber for multifunctional composites. Compos Sci Technol 2008;68(7–8):1911–8. http://dx.doi.org/10.1016/j.compscitech.2007.12.017.
[19] Wilkie WK, Bryant RG, High JW, Fox RL, Hellbaum RF, Jalink A. Jr. et al., Low-cost piezocomposite actuator for structural control applications. In: SPIE's 7th Annual International Symposium on Smart Structures and Materials, International Society for Optics and Photonics, pp. 323–334.
[20] High JW, Wilkie WK. Method of fabricating NASA-standard macro-fiber composite piezoelectric actuators.
[21] Cen L, Erturk A. Bio-inspired aquatic robotics by untethered piezohydroelastic actuation. Bioinspiration and Biomimetics 2013;8(1):016006.
[22] Kim DK, Han JH. Smart flapping wing using macrofiber composite actuators. In: Smart Structures and Materials, International Society for Optics and Photonics, p. 61730F.
[23] Kim DK, Kim HI, Han JH, Kwon KJ. Experimental investigation on the aerodynamic characteristics of a bio-mimetic flapping wing with macro-fiber composites, J Intell Mater Syst Struct.
[24] Paradies R, Ciresa P. Active wing design with integrated flight control using piezoelectric macro fiber composites. Smart Mater Struct 2009;18(3):035010.
[25] Bilgen O, Kochersberger KB, Inman DJ, Ohanian OJ. Novel, bidirectional, variable-camber airfoil via macro-fiber composite actuators. J Aircraft 2010;47(1):303–14.
[26] Browning JS. F-16 ventral fin buffet alleviation using piezoelectric actuators, Thesis (2009).
[27] Cha Y, Kim H, Porfiri M. Energy harvesting from underwater base excitation of a piezoelectric composite beam. Smart Mater Struct 2013;22(11):115026.
[28] Shahab S, Erturk A. Underwater dynamic actuation of macro-fiber composite flaps with different aspect ratios: Electrohydroelastic modeling, testing, and characterization. In: ASME 2014 Conference on Smart Materials, Adaptive Structures and Intelligent Systems, American Society of Mechanical Engineers, p. V002T06A007.
[29] Shahab S, Erturk A. Electrohydroelastic dynamics of macro-fiber composites for underwater energy harvesting from base excitation. In: SPIE Smart Structures and Materials + Nondestructive Evaluation and Health Monitoring, Vol. 9057, International Society for Optics and Photonics, p. 90570C.
[30] Shahab S, Erturk A. Unified electrohydroelastic investigation of underwater energy harvesting and dynamic actuation by incorporating Morison's equation. In: SPIE Smart Structures and Materials + Nondestructive Evaluation and Health Monitoring, International Society for Optics and Photonics, p. 94310C.
[31] Cha Y, Chae W, Kim H, Walcott H, Peterson SD, Porfiri M. Energy harvesting from a piezoelectric biomimetic fish tail. Renewable Energy 2016;86:449–58.
[32] Williams RB, Grimsley BW, Inman DJ, Wilkie WK. Manufacturing and mechanics-based characterization of macro fiber composite actuators. In: ASME 2002 International mechanical engineering congress and exposition, American Society of Mechanical Engineers, pp. 79–89.
[33] Williams RB, Inman DJ, Schultz MR, Hyer MW, Wilkie WK. Nonlinear tensile and shear behavior of macro fiber composite actuators. J Compos Mater 2004;38(10):855–69.
[34] Williams RB, Inman DJ, Wilkie WK. Temperature-dependent thermoelastic properties for macro fiber composite actuators. J Therm Stress 2004;27(10):903–15.
[35] Deraemaeker A, Nasser H, Benjeddou A, Preumont A. Mixing rules for the piezoelectric properties of macro fiber composites. J Intell Mater Syst Struct 2009;20(12):1475–82. http://dx.doi.org/10.1177/1045389x09335615.
[36] Shahab S, Erturk A. Coupling of experimentally validated electroelastic dynamics and mixing rules formulation for macro-fiber composite piezoelectric structures. J Intell Mater Syst Struct 2017;28(12):1575–88.
[37] Leadenham S, Erturk A. Unified nonlinear electroelastic dynamics of a bimorph piezoelectric cantilever for energy harvesting, sensing, and actuation. Nonlinear Dyn 2015;79(3):1727–43.
[38] Goldschmidtboeing F, Eichhorn C, Wischke M, Kroener M, Woias P. The influence of ferroelastic hysteresis on mechanically excited PZT cantilever beams. In: Proceedings of the 11th International Workshop on Micro and Nanotechnology for Power Generation and Energy Conversion Applications, pp. 114–117.
[39] Tan D, Erturk A. In vacuo elastodynamics of a flexible cantilever for wideband energy harvesting. In: SPIE Smart Structures and Materials + Nondestructive Evaluation and Health Monitoring, International Society for Optics and Photonics.
[40] Nayfeh AH, Mook DT. Nonlinear oscillations. John Wiley and Sons; 2008.
[41] Malatkar P. Nonlinear vibrations of cantilever beams and plates, Thesis (2003).
[42] Crespo da Silva MRM, Glynn CC. Nonlinear flexural-flexural-torsional dynamics of inextensional beams. i. equations of motion. Journal of Structural Mechanics 1978;6(4):437–48. http://dx.doi.org/10.1080/03601217808907348.
[43] Nayfeh AH, Pai PF. Non-linear non-planar parametric responses of an inextensional beam. Int J Non-Linear Mech 1989;24(2):139–58. http://dx.doi.org/10.1016/0020-7462(89)90005-X.
[44] Li S, Cao W, Cross LE. The extrinsic nature of nonlinear behavior observed in lead zirconate titanate ferroelectric ceramic. J Appl Phys 1991;69(10):7219–24. http://dx.doi.org/10.1063/1.347616.